SUPERCONDUCTIVITY

Nematic spin correlations in the tetragonal state of uniaxial-strained $BaFe_{2-x}Ni_xAs_2$

Xingye Lu,[1] J. T. Park,[2] Rui Zhang,[1] Huiqian Luo,[1] Andriy H. Nevidomskyy,[3] Qimiao Si,[3] Pengcheng Dai[3,1]*

Understanding the microscopic origins of electronic phases in high-transition temperature (high-T_c) superconductors is important for elucidating the mechanism of superconductivity. In the paramagnetic tetragonal phase of $BaFe_{2-x}T_xAs_2$ (where T is Co or Ni) iron pnictides, an in-plane resistivity anisotropy has been observed. Here, we use inelastic neutron scattering to show that low-energy spin excitations in these materials change from fourfold symmetric to twofold symmetric at temperatures corresponding to the onset of the in-plane resistivity anisotropy. Because resistivity and spin excitation anisotropies both vanish near optimal superconductivity, we conclude that they are likely intimately connected.

Superconductivity in iron pnictides can be induced by electron or hole-doping of their antiferromagnetic (AF) parent compounds (*1*–*6*). The parent compounds exhibit a tetragonal-to-orthorhombic structural phase transition at temperature T_s, followed by a paramagnetic to AF phase transition at T_N ($T_s \geq T_N$) (*4*–*6*). An in-plane resistivity anisotropy has been observed in uniaxially strained iron pnictides $BaFe_{2-x}T_xAs_2$ (where T is Co or Ni) above T_s (*7*–*9*). This anisotropy vanishes near optimal superconductivity and has been suggested as a signature of the spin nematic phase that breaks the in-plane fourfold rotational symmetry (C_4) of the underlying tetragonal lattice (*10*–*14*). However, such interpretation was put in doubt by recent scanning tunneling microscopy (*15*) and transport (*16*) measurements, which suggest that the resistivity anisotropy in Co-doped $BaFe_2As_2$ arises from Co-impurity scattering and is not an intrinsic property of these materials. On the other hand, angle-resolved photoemission spectroscopy (ARPES) measurements found that the onset of a splitting in energy between two orthogonal bands with dominant d_{xz} and d_{yz} character in the uniaxial-strain detwinned samples at a temperature above T_s (*17*, *18*), thereby suggesting the involvement of the orbital channel in the nematic phase (*19*–*22*). Here, we use inelastic neutron scattering (INS) to show that low-energy spin excitations in $BaFe_{2-x}Ni_xAs_2$ (x = 0, 0.085, and 0.12) (*23*, *24*) change from fourfold symmetric to twofold symmetric in the uniaxial-strained tetragonal phase at temperatures corresponding to the onset of the in-plane resistivity anisotropy.

The magnetic order of the parent compounds of iron pnictide superconductors is collinear, with the ordered moment aligned antiferromagnetically along the a_o axis of the orthorhombic lattice (Fig. 1A), and occurs at a temperature just below $T_s \approx T_N \approx 138$ K for $BaFe_2As_2$ (*5*, *6*). Because of the twinning effect in the orthorhombic state, AF Bragg peaks from the twinned domains appear at the (±1, 0) and (0, ±1) in-plane positions in reciprocal space (Fig. 1B) (*3*). Therefore, one needs to prepare single domain samples by applying a uniaxial pressure (strain) along one axis of the orthorhombic lattice to probe the intrinsic electronic properties of the system (*7*–*9*). Indeed, transport measurements on uniaxial-strain detwinned samples of electron-underdoped $BaFe_{2-x}T_xAs_2$ (*7*–*10*) reveal clear in-plane resistivity anisotropy even above the zero pressure T_c, T_N, and T_s (Fig. 1C).

To search for a possible spin nematic phase (*12*–*14*), we carried out INS experiments in uniaxial-strain detwinned parent compound $BaFe_2As_2$ (T_N = 138 K), electron-underdoped superconducting $BaFe_{1.915}Ni_{0.085}As_2$ (T_c = 16.5 K, T_N = 44 K), and electron-overdoped superconducting $BaFe_{1.88}Ni_{0.12}As_2$ (T_c = 18.6 K, tetragonal structure with no static AF order) (Fig. 1C) (*23*, *24*) using a thermal triple-axis spectrometer. Horizontally and vertically curved pyrolytic graphite (PG) crystals were used as a monochromator and analyzer. To eliminate contamination from epithermal or higher-order neutrons, a sapphire filter was added before the monochromator, and two PG filters were installed before the analyzer. All measurements were done with a fixed final wave vector, k_f = 2.662 Å^{-1}. Our annealed square-shaped single crystals of $BaFe_2As_2$ (~120 mg), $BaFe_{1.915}Ni_{0.085}As_2$ (~220 mg), and $BaFe_{1.88}Ni_{0.12}As_2$ (~448 mg) were mounted inside aluminum-based sample holders with a uniaxial pressure of $P \approx 15$ MPa, ~7 MPa, and ~7 MPa, respectively, applied along the a_o/b_o axes direction (fig. S1A) (*25*–*27*). We define momentum transfer $\mathbf{Q}$ in three-dimensional reciprocal space in Å^{-1} as $\mathbf{Q} = H\boldsymbol{a}^* + K\boldsymbol{b}^* + L\boldsymbol{c}^*$, where H, K, and L are Miller indices and $\boldsymbol{a}^* = \hat{\mathbf{a}}_o 2\pi/a_o$, $\boldsymbol{b}^* = \hat{\mathbf{b}}_o 2\pi/b_o$, and $\boldsymbol{c}^* = \hat{\mathbf{c}} 2\pi/c_o$. In the AF ordered state of a 100% detwinned sample, the AF Bragg peaks should occur at (±1, 0, L) (L = 1, 3, 5, ⋯) positions in reciprocal space. In addition, the low-energy spin waves should only stem from the (±1, 0) positions with no signal at the (0, ±1) positions (*26*, *27*). By contrast, in the paramagnetic tetragonal phase ($T > T_s \geq T_N$) one would expect the spin excitations at the (±1, 0) and (0, ±1) positions to have equal intensities (*12*, *27*).

The results of our INS experiments on uniaxial-strain detwinned $BaFe_{2-x}Ni_xAs_2$ are summarized in Fig. 1C. The square red symbols indicate the temperature below which spin excitations at an energy transfer of E = 6 meV exhibit a difference in intensity between the (±1, 0) and (0, ±1) positions for undoped and electron underdoped $BaFe_{2-x}Ni_xAs_2$. For electron overdoped $BaFe_{1.88}Ni_{0.12}As_2$, the same uniaxial pressure has no effect on spin excitations at wave vectors (±1, 0) and (0, ±1) (*27*). A comparison to the transport measurements (*10*) in Fig. 1C indicates that the resistivity anisotropy occurs near the spin excitation anisotropy temperature T^* determined from INS.

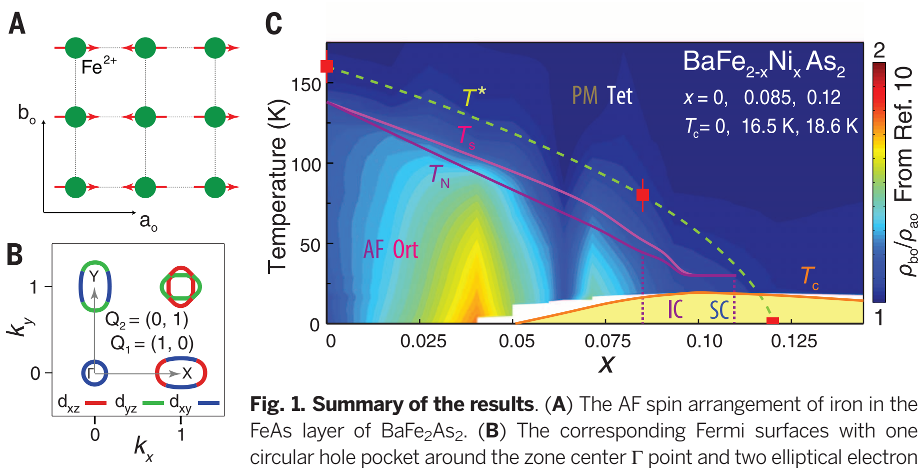

Fig. 1. Summary of the results. (**A**) The AF spin arrangement of iron in the FeAs layer of $BaFe_2As_2$. (**B**) The corresponding Fermi surfaces with one circular hole pocket around the zone center Γ point and two elliptical electron pockets at X and Y points (*3*). (**C**) The electronic phase diagram of $BaFe_{2-x}Ni_xAs_2$ from resistivity anisotropy ratio ρ_{bo}/ρ_{ao} obtained under uniaxial pressure (*10*). The spin excitation anisotropy temperatures are marked as T^*. The AF orthorhombic (Ort), incommensurate AF (IC) (*23*), paramagnetic tetragonal (PM Tet), and superconductivity (SC) phases are marked.

[1]Beijing National Laboratory for Condensed Matter Physics, Institute of Physics, Chinese Academy of Sciences, Beijing 100190, China. [2]Heinz Maier-Leibnitz Zentrum (MLZ), Technische Universität München, D-85748 Garching, Germany. [3]Department of Physics and Astronomy, Rice University, Houston, TX 77005, USA.
*Corresponding author. E-mail: pdai@rice.edu

Given that our experiments are performed in uniaxial-strain detwinned samples, it is important to establish how the structural and magnetic transition temperatures are affected by the applied pressure. Figure S2A compares the temperature dependence of the magnetic order parameters at (1, 0, 1)/(0, 1, 1) for $BaFe_2As_2$ in zero pressure (green symbols) and under uniaxial strain (red and blue symbols). We find that the $BaFe_2As_2$ sample is essentially 100% detwinned under the applied uniaxial strain without altering T_N (*27*). Similarly, the electron underdoped $BaFe_{1.915}Ni_{0.085}As_2$ is about 80% detwinned and has $T_N \approx 44$ K, unchanged from the zero-pressure case (fig. S2B) (*27*). To investigate whether the tetragonal-to-orthorhombic structural phase transition in $BaFe_{2-x}Ni_xAs_2$ is affected by uniaxial strain, we plot the temperature dependence of the (2, −2, 0) nuclear Bragg peak of $BaFe_2As_2$; both zero pressure (fig. S2C) and detwinned samples (fig. S2D) exhibit a steplike feature at $T_s \approx 138$ K resulting from the vanishing neutron extinction effect due to the tetragonal-to-orthorhombic structural transition (*28*, *29*).

In previous spin-wave measurements on twinned $BaFe_2As_2$, a spin gap of ~10 meV was found at the (1, 0, 1) and (0, 1, 1) positions (*30*). To probe spin excitations at the same wave vectors in the detwinned $BaFe_2As_2$, we aligned the sample in the [1, 0, 1] × [0, 1, 1] scattering plane (*27*). Figure 2, A, C, and E, shows constant-energy scans centered at (1, 0, 1) approximately along the [1, *K*, 1] direction. Whereas spin waves at (1, 0, 1) are clearly gapped at E = 6 meV in the AF ordered state (T = 3 K) in Fig. 2A, they are well defined at E = 15 meV (Fig. 2C) and 19 meV (Fig. 2E), in line with the previous report (*31*). We find no evidence for spin waves at E = 6, 15, and 19 meV at (0, 1, 1) (Fig. 2, B, D, and F, respectively), which is consistent with a nearly 100% detwinned $BaFe_2As_2$. On warming the system to the paramagnetic tetragonal state at T = 154 K, the spin gap disappears and the E = 6 meV spin excitations at the AF wave vector (1, 0, 1) are clearly stronger than those at (0, 1, 1) (Fig. 2, A and B) (*27*).

To quantitatively study the energy dependence of the spin excitation anisotropy in $BaFe_2As_2$ at a temperature above T_s, we plot in Fig. 3A the energy scans at wave vectors (1, 0, 1) and (0, 1, 1) and their corresponding backgrounds at T = 154 K (*27*). The background-subtracted scattering at (1, 0, 1) is consistently higher than that at (0, 1, 1) (Fig. 3, C and E, left inset). When we warm up to T = 189 K, the corresponding energy scans (Fig. 3B) and the signals above background (Fig. 3D) reveal that the differences at these two wave vectors disappear (Fig. 3E, left inset). Figure 3E shows the temperature dependence of the spin excitations (signal above background scattering) across T_N and T_s. In the AF ordered state, we see only spin waves from the wave vector (1, 0, 1). On warming to the paramagnetic tetragonal state above T_N and T_s, we see clear differences between (1, 0, 1) and (0, 1, 1) that vanish above ~160 K, the same temperature below which anisotropy is observed in the in-plane resistivity (Fig. 3E, right inset) (*32*). We conclude that the fourfold to twofold symmetry change in spin excitations in $BaFe_2As_2$ occurs alongside the resistivity anisotropy.

To see if spin excitations in superconducting $BaFe_{1.915}Ni_{0.085}As_2$ also exhibit the fourfold to twofold symmetry transition, we study the temperature dependence of the E = 6 meV spin excitations at the (1, 0, 1) and (0, 1, 1) wave vectors. In previous INS experiments on twinned $BaFe_{1.92}Ni_{0.08}As_2$, a neutron spin resonance was found near $E \approx 6$ meV (*33*). Figure 4, A and C, shows approximate transverse and radial scans through (1, 0, 1) at various temperatures; one can clearly see the superconductivity-induced intensity enhancement from 48 K to 8 K. The corresponding scans through (0, 1, 1) (Fig. 4, B and D) have weaker intensity than those at (1, 0, 1). Figure 4E shows the temperature dependence of the magnetic scattering at (1, 0, 1) and (0, 1, 1). Consistent with constant-energy scans in Fig. 4, A to D, the scattering at (1, 0, 1) is considerably stronger than that at (0, 1, 1) above T_c. On warming through T_N and T_s (*24*), the spin excitation anisotropy between (1, 0, 1) and (0, 1, 1) becomes smaller, but reveals no dramatic change. The anisotropy disappears around $T^* \sim 80$ K, well above T_N and T_s (Fig. 4, E and F) but similar to the point of vanishing in-plane resistivity anisotropy (*10*). Finally, we find that uniaxial strain does not break the C_4 rotational symmetry of the spin excitations in electron-overdoped $BaFe_{1.88}Ni_{0.12}As_2$ (fig. S5) (*27*). In this compound, resistivity shows no a_o/b_o anisotropy (*10*).

Conceptually, once the C_4 symmetry of the electronic ground state is broken, the electronic anisotropy will couple linearly to the orthorhombic lattice distortion $\epsilon = a_o - b_o$, so that the C_4 nematic transition should coincide with the tetragonal-to-orthorhombic transition at temperature T_s (*12*–*14*). How do we then understand the region $T_s < T < T^*$ in which the low-energy spin excitations develop an anisotropy? Theoretically, this is best understood in terms of the effective action for the electronic nematic order parameter Δ and magnetization $\mathbf{M}_{1/2}$ of the interpenetrating Néel sublattices (*14*, *34*, *35*).

$$S_{\text{eff}}[\Delta,\mathbf{M}] = S_0\left[\mathbf{M}_1^2,\mathbf{M}_2^2\right] + \iint d\mathbf{q}d\omega\left[\alpha^{-1}(\mathbf{q},\omega)|\Delta|^2 + v|\Delta|^4 - g\left(\mathbf{M}_1\cdot\mathbf{M}_2\right)\Delta - \lambda\epsilon\Delta\right] + C_s\epsilon^2/2 \quad (1)$$

Here, S_0 is defined as part of the action that does not contain nematic correlations $\left(\mathbf{M}_1\cdot\mathbf{M}_2\right)$ (*36*), which have been decoupled in terms of the bosonic field $\Delta(\mathbf{q},\omega)$ characterized by the nematic susceptibility $\alpha(\mathbf{q},\omega)$, where energy $E = \hbar\omega$, g is a linear coupling between the Ising-spin variable

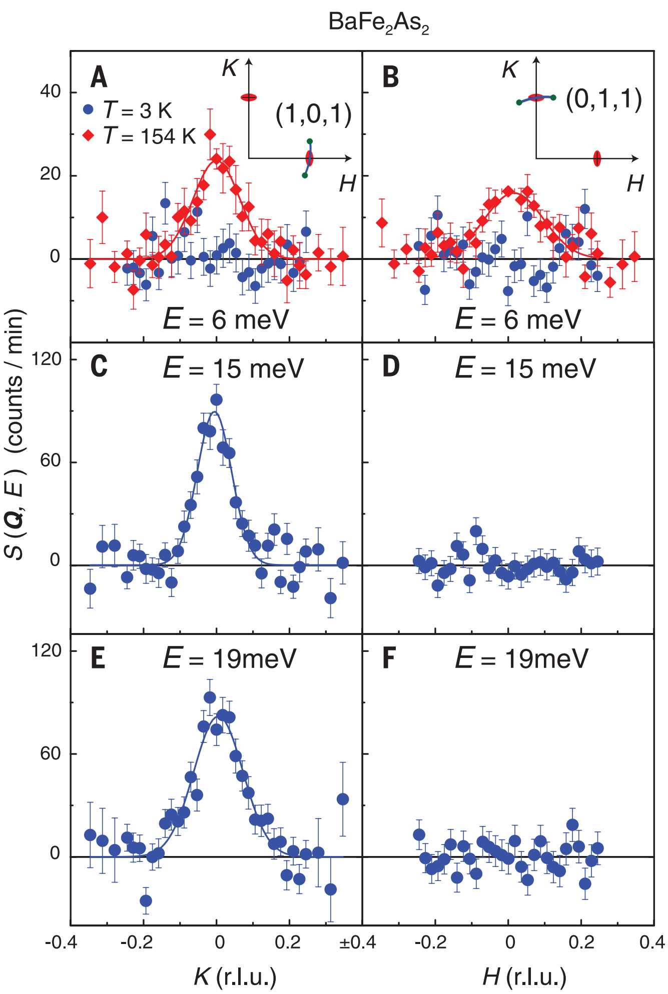

Fig. 2. Constant-energy scans for detwinned $BaFe_2As_2$. The E = 6 meV rocking scans measured at T = 3 K in the AF ordered state and T = 154 K in the paramagnetic tetragonal state centered at (**A**) (1, 0, 1) and (**B**) (0, 1, 1). T = 3 K scans at E = 15 meV for (**C**) (1, 0, 1) and (**D**) (0, 1, 1) and at E = 19 meV for (**E**) (1, 0, 1) and (**F**) (0, 1, 1). The in-plane projected trajectories of the rocking scans crossing (1, 0, 1) and (0, 1, 1) are illustrated by blue lines in the insets of (A) and (B), respectively. Solid lines are Gaussian fits.

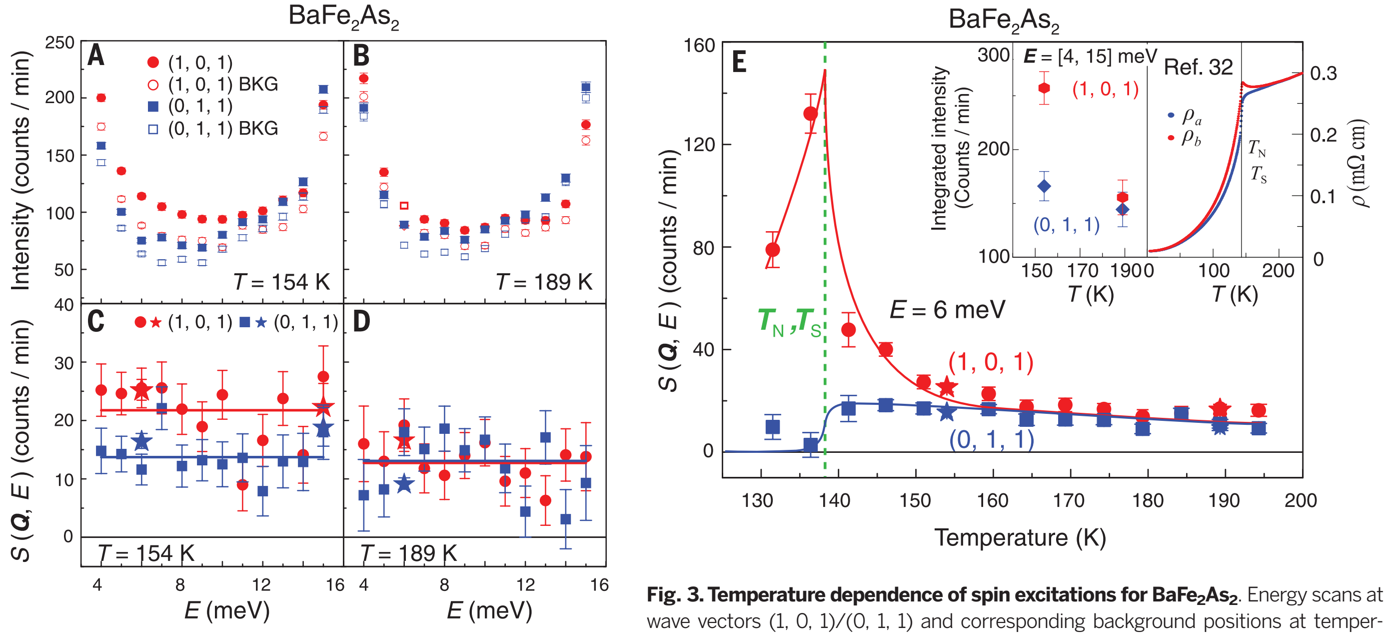

Fig. 3. Temperature dependence of spin excitations for BaFe$_2$As$_2$. Energy scans at wave vectors (1, 0, 1)/(0, 1, 1) and corresponding background positions at temperatures above T_S: (**A**) T = 154 K and (**B**) 189 K. (**C** and **D**) Magnetic scattering after subtracting the backgrounds. The solid lines are constant line fits. (**E**) Temperature dependence of the spin excitations at E = 6 meV for (1, 0, 1) and (0, 1, 1). The anisotropy in spin excitations vanishes around T = 160 ± 10 K. The data marked by filled squares and dots in (C) to (E) were obtained by subtracting the corresponding backgrounds. For each temperature, the background intensities at **Q** = (1, 0, 1) and (0, 1, 1) were obtained by averaging the data at the two wave vectors marked by green dots in the insets of Fig. 2, A and B, respectively. The data denoted by filled stars in (C) to (E) were obtained by fitting the rocking scans for E = 6 and 15 meV at different temperatures. The solid lines in (E) are guides to the eye. The left inset in (E) shows temperature dependence of the integrated intensity from 4 to 15 K; the right inset shows temperature dependence of the resistivity from (*32*).

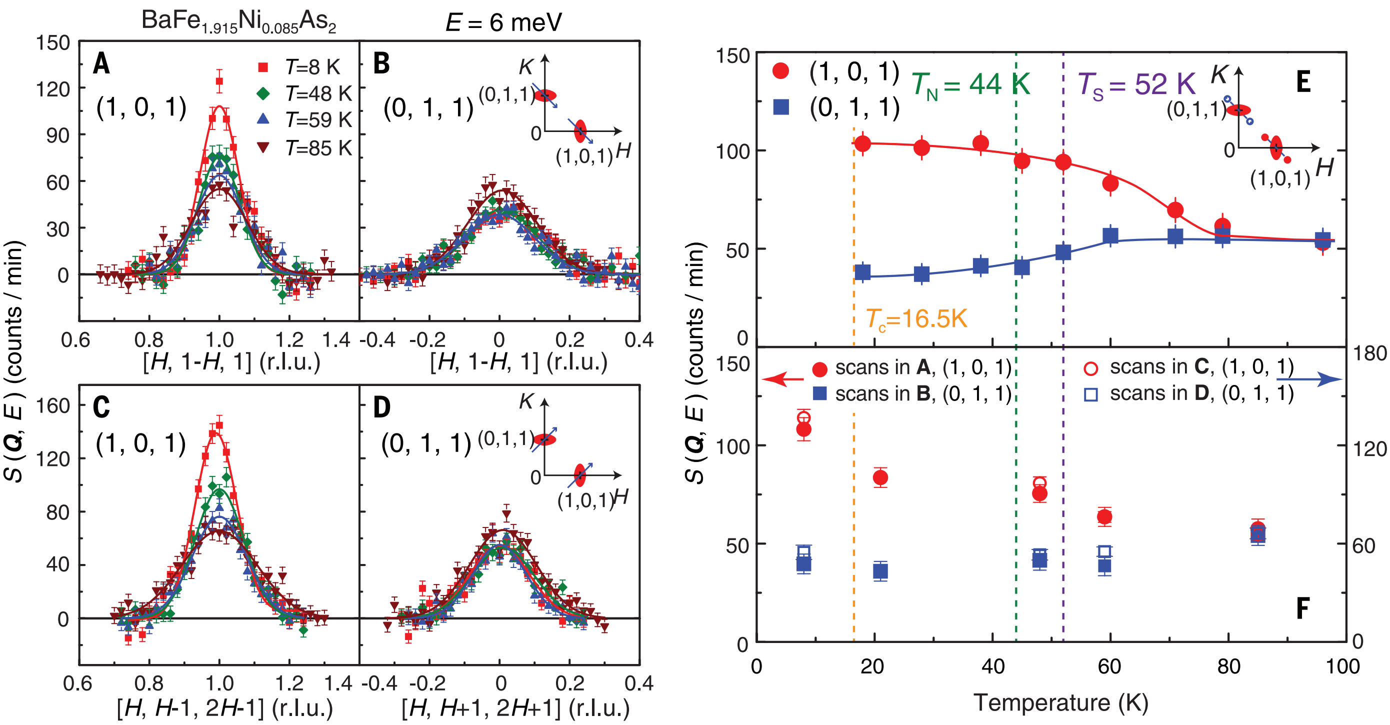

Fig. 4. Temperature dependence of spin excitations for BaFe$_{1.915}$Ni$_{0.085}$As$_2$. Background-subtracted **Q** scans at E = 6 meV around (**A** and **C**) (1, 0, 1) and (**B** and **D**) (0, 1, 1). The trajectory of the scans (blue line) crossing spin excitations (red ellipses) are illustrated in the insets of (B) and (D). (**E** and **F**) Temperature dependence of the spin excitations at (1, 0, 1) and (0, 1, 1) at E = 6 meV. The data in (E) were obtained by subtracting the background intensity from the peak intensity at every temperature; the data in (F) were obtained by fitting the **Q** scans. The wave vectors used for calculating the background (blue circles and red dots) are shown in the inset of (E). The solid curves in (A) to (D) are Gaussian fits and in (E) are guides to the eye. The temperatures for structural (purple), magnetic (blue), and SC (orange) transitions are marked by vertical dashed lines (*24*).

and the bosonic field, v is the quartic coupling among the bosonic fields, λ is the linear coupling between the bosonic field and the orthorhombic lattice distortion ϵ, and $\mathbf{q}$ is the momentum transfer within one Brillouin zone. Minimizing the action with respect to ϵ, we arrive at $\epsilon = \lambda\langle\Delta\rangle/C_s$, where C_s is the shear modulus. In other words, the orthorhombic lattice distortion is proportional to the nematic order parameter $\langle\Delta\rangle$, and both are expected to develop nonzero expectation values below T_s (*12–14*). However, the nematic field Δ undergoes fluctuations in the tetragonal phase above T_s while lattice distortion ϵ remains zero. These fluctuations will be observable in dynamic quantities, such as the finite-energy spin fluctuations, and in transport measurements. We therefore conclude that the scale T^*, below which we observe anisotropy of low-energy spin fluctuations (Figs. 3E, 4E, and 4F) and where the resistivity anisotropy is observed (Fig. 3E, right inset), marks a typical range of the nematic fluctuations.

Several remarks are in order. First, the applied uniaxial pressure used to detwin the samples will induce a finite value of ϵ at any temperature, so that strictly speaking, the structural transition at T_s will be rendered a crossover. In practice, however, the applied pressure is too small to cause a perceptible lattice distortion, which is why the transition temperature T_s, as determined from the extinction effect of the nuclear (2, –2, 0) Bragg peak remains unchanged from the zero-pressure case [fig. S2, B and D] (*26*, *27*). On the other hand, the extent of nematic fluctuations may be sensitive to the shear strain, in agreement with the reported increase of T^* (as determined from resistivity anisotropy) with the uniaxial pressure (*37*). Second, in Eq. 1 the variable Δ could equally signify the orbital order $\Delta \propto (n_{xz} - n_{yz})$ which lifts the degeneracy between the Fe d_{xz} and d_{yz} orbitals. In fact, the two order parameters will couple linearly to each other, $\left(\mathbf{M}_1 \cdot \mathbf{M}_2\right) \propto (n_{xz} - n_{yz})$, so that both will develop a nonzero value below T_s. In this respect, our findings are also consistent with the recent ARPES finding of an orbital ordering (*17*, *18*) in $BaFe_2As_2$. This underlines the complementarity of the spin-nematic and orbital descriptions of the C_4 symmetry breaking. Third, in the nearly optimally electron-doped superconductor, we observe anisotropy of the low-lying spin excitations in the tetragonal phase $T_s < T < T^*$, even though the orbital order is no longer detectable by ARPES (*17*, *18*). This is consistent with the absence of a static nematic order $\langle\Delta\rangle = 0$ above T_s, whereas the observed spin anisotropy originates from Ising-nematic fluctuations. Because T_s is considerably suppressed for this doping, these fluctuations are quantum rather than thermal: They persist beyond the immediate vicinity of T_s, and the associated spin anisotropy should have sizable dependence on frequency that can be probed by future experiments. Fourth, when resistivity anisotropy under uniaxial strain disappears in the electron-overdoped sample (*10*), the uniaxial-strain–induced spin excitation anisotropy also vanishes (Fig. 1E and fig. S5), which suggests a direct connection between these two phenomena. Finally, our measurements in the spin channel do not necessarily signal a thermodynamic order at the temperature T^*. Rather, T^* likely signals a crossover, whereas the true nematic transition occurs at T_s (*9*). This implies that a static order above T_s inferred from recent measurements of magnetic torque anisotropy in the isovalent $BaFe_2As_{2-x}P_x$ (*38*) is most likely not in the spin channel accessible to the inelastic neutron scattering. A static order in other channels—such as, for instance, an octupolar order—would, however, not contradict our observations.

REFERENCES AND NOTES

1. Y. Kamihara, T. Watanabe, M. Hirano, H. Hosono, *J. Am. Chem. Soc.* **130**, 3296–3297 (2008).
2. G. R. Stewart, *Rev. Mod. Phys.* **83**, 1589–1652 (2011).
3. P. C. Dai, J. Hu, E. Dagotto, *Nat. Phys.* **8**, 709–718 (2012).
4. C. de la Cruz, Q. Huang, J. W. Lynn, J. Li, W. Ratcliff II J. L. Zarestky *et al.*, *Nature* **453**, 899–902 (2008).
5. Q. Huang *et al.*, *Phys. Rev. Lett.* **101**, 257003 (2008).
6. M. G. Kim *et al.*, *Phys. Rev. B* **83**, 134522 (2011).
7. J. H. Chu *et al.*, *Science* **329**, 824–826 (2010).
8. M. A. Tanatar *et al.*, *Phys. Rev. B* **81**, 184508 (2010).
9. J. H. Chu, H.-H. Kuo, J. G. Analytis, I. R. Fisher, *Science* **337**, 710–712 (2012).
10. I. R. Fisher, L. Degiorgi, Z. X. Shen, *Rep. Prog. Phys.* **74**, 124506 (2011).
11. E. Fradkin, S. A. Kivelson, M. J. Lawler, J. P. Eisenstein, A. P. Mackenzie, *Annu. Rev. Condens. Matter Phys.* **1**, 153–178 (2010).
12. R. M. Fernandes, A. V. Chubukov, J. Schmalian, *Nat. Phys.* **10**, 97–104 (2014).
13. C. Fang, H. Yao, W.-F. Tsai, J. P. Hu, S. A. Kivelson, *Phys. Rev. B* **77**, 224509 (2008).
14. J. Dai, Q. Si, J. X. Zhu, E. Abrahams, *Proc. Natl. Acad. Sci. U.S.A.* **106**, 4118–4121 (2009).
15. M. P. Allan *et al.*, *Nat. Phys.* **9**, 220–224 (2013).
16. S. Ishida *et al.*, *Phys. Rev. Lett.* **110**, 207001 (2013).
17. M. Yi *et al.*, *Proc. Natl. Acad. Sci. U.S.A.* **108**, 6878–6883 (2011).
18. Y. Zhang *et al.*, *Phys. Rev. B* **85**, 085121 (2012).
19. C. C. Lee, W. G. Yin, W. Ku, *Phys. Rev. Lett.* **103**, 267001 (2009).
20. F. Krüger, S. Kumar, J. Zaanen, J. van den Brink, *Phys. Rev. B* **79**, 054504 (2009).
21. W. C. Lv, J. S. Wu, P. Phillips, *Phys. Rev. B* **80**, 224506 (2009).
22. C.-C. Chen *et al.*, *Phys. Rev. B* **82**, 100504 (2010).
23. H. Luo *et al.*, *Phys. Rev. Lett.* **108**, 247002 (2012).
24. X. Lu *et al.*, *Phys. Rev. Lett.* **110**, 257001 (2013).
25. C. Dhital *et al.*, *Phys. Rev. Lett.* **108**, 087001 (2012).
26. Yu. Song *et al.*, *Phys. Rev. B* **87**, 184511 (2013).
27. Materials and methods are available as supplementary materials on *Science* Online.
28. C. Lester *et al.*, *Phys. Rev. B* **79**, 144523 (2009).
29. A. Kreyssig *et al.*, *Phys. Rev. B* **81**, 134512 (2010).
30. J. T. Park *et al.*, *Phys. Rev. B* **86**, 024437 (2012).
31. L. W. Harriger *et al.*, *Phys. Rev. B* **84**, 054544 (2011).
32. M. Nakajima *et al.*, *Phys. Rev. Lett.* **109**, 217003 (2012).
33. M. Y. Wang *et al.*, *Phys. Rev. B* **83**, 094516 (2011).
34. P. Chandra, P. Coleman, A. I. Larkin, *Phys. Rev. Lett.* **64**, 88–91 (1990).
35. R. M. Fernandes, J. Schmalian, *Supercond. Sci. Technol.* **25**, 084005 (2012).
36. The Ginzburg–Landau action up to the 4th power of $\mathbf{M}_{1/2}$: $S_0\left[\mathbf{M}_1^2, \mathbf{M}_2^2\right] = \iint d\mathbf{q}d\omega\ \left(r_0 + \mathbf{q}^2 + \gamma|\omega|\right)\left(\mathbf{M}_1^2 + \mathbf{M}_2^2\right) + u\left(\mathbf{M}_1^2 + \mathbf{M}_2^2\right)^2$, where $r_0 \propto T - T_N$ describes distance from the Néel point.
37. H.-H. Kuo *et al.*, *Phys. Rev. B* **84**, 054540 (2011).
38. S. Kasahara *et al.*, *Nature* **486**, 382–385 (2012).

ACKNOWLEDGMENTS

The work at the Institute of Physics, Chinese Academy of Sciences is supported by Ministry of Science and Technology of China (973 project: 2012CB821400 and 2011CBA00110), National Natural Science Foundation of China and China Academy of Engineering Physics. The work at Rice is supported by the U.S. NSF-DMR-1308603 and DMR-1362219 (P.D.), by Robert A. Welch Foundation grant no. C-1839 (P.D.), C-1818 (A.H.N.), and no. C-1411 (Q.S.), and by the U.S. NSF-DMR-1309531 and the Alexander von Humboldt Foundation (Q.S.). A.H.N. and Q.S. acknowledge the hospitality of the Aspen Center for Physics, where support was provided by NSF grant PHYS-1066293.

SUPPLEMENTARY MATERIALS

www.sciencemag.org/content/345/6197/657/suppl/DC1
Materials and Methods
Figs. S1 to S5
References (*39*, *40*)

6 February 2014; accepted 25 June 2014
Published online 31 July 2014;
10.1126/science.1251853

SELECTIVE ATTENTION

Long-range and local circuits for top-down modulation of visual cortex processing

Siyu Zhang,[1] Min Xu,[1] Tsukasa Kamigaki,[1] Johnny Phong Hoang Do,[1] Wei-Cheng Chang,[1] Sean Jenvay,[1] Kazunari Miyamichi,[2]* Liqun Luo,[2] Yang Dan[1]†

Top-down modulation of sensory processing allows the animal to select inputs most relevant to current tasks. We found that the cingulate (Cg) region of the mouse frontal cortex powerfully influences sensory processing in the primary visual cortex (V1) through long-range projections that activate local γ-aminobutyric acid–ergic (GABAergic) circuits. Optogenetic activation of Cg neurons enhanced V1 neuron responses and improved visual discrimination. Focal activation of Cg axons in V1 caused a response increase at the activation site but a decrease at nearby locations (center-surround modulation). Whereas somatostatin-positive GABAergic interneurons contributed preferentially to surround suppression, vasoactive intestinal peptide-positive interneurons were crucial for center facilitation. Long-range corticocortical projections thus act through local microcircuits to exert spatially specific top-down modulation of sensory processing.

Sensory processing is strongly modulated by the animal's behavioral state. A well-known example is top-down attention, a powerful mechanism for selective processing of behaviorally relevant information and filtering out irrelevant stimuli. In visual cortical areas, many neurons exhibit enhanced responses to attended stimuli (*1–4*). Several frontal and parietal cortical regions have been implicated as the sources of top-down modulation

Materials and Methods

Sample preparation

$BaFe_{2-x}Ni_xAs_2$ single crystals were grown with self-flux method. The basic sample characterizations were described in our previous study [39]. Large single crystals with less flux were selected and annealed in Ba_2As_3 for several days. The tetragonal [1,1,0] direction of annealed crystals was determined by X-ray Laue diffraction. The crystals were cut into rectangular pieces along the [1,1,0] and [1,-1,0] directions by high precision wire saw.

Samples used in this report are $BaFe_2As_2$ ($T_N = T_s = 138$ K), electron-underdoped superconducting $BaFe_{1.915}Ni_{0.085}As_2$ ($T_c = 16.5$K, $T_N = 44$ K, $T_s = 52$ K) and electron-overdoped $BaFe_{1.88}Ni_{0.12}As_2$ ($T_c = 18.6$ K).

Device for sample detwinning

The device for sample detwinning was made of 6061 aluminum alloy with low neutron incoherent scattering cross section. As shown in Fig. S1A, uniaxial pressure can be applied by a spring along orthorhombic [0,1,0] direction by tuning the screw in one end. The pressure can be calculated by the known elasticity coefficient ($k = 10.5$ N/mm) and the compression of the spring (Δx). The elasticity coefficient was measured in our lab, as shown in Fig. S1B. Take $BaFe_{1.915}Ni_{0.085}As_2$ as an example, the sample size is 7.97mm*6.42mm*0.70mm. Thus the sectional area we applied pressure were 7.97*0.7=5.58 mm^2. The compression of the spring in the experiment was about 3.5 mm. A simple calculation gives a pressure ~6.6 MPa. However, since the pressure calibrations were done at room temperature and we do not know the elasticity coefficient of the spring at low temperatures, the applied pressure was only a rough estimate. What we do know is that the applied pressure is sufficient to detwin the sample. In Fig. S1A, the device is mounted on a supporting sample holder to align the crystal in the [1,0, 1]×[0,1,1] scattering plane (see Fig. S1C), where the spin excitations at $\mathbf{Q}_{\mathbf{AF}} = (1,0,1)$ and (0,1,1) can be measured and compared directly.

Sample detwinning

Our neutron scattering experiments were carried out using the PUMA thermal triple-axis spectrometer at the MLZ in Garching, Germany. The efficiency of sample detwinning can be checked by comparing the intensity of the magnetic Bragg peaks at (1,0,1) and (0,1,1). For a fully detwinned sample, magnetic elastic scattering is expected to appear only at the antiferromagnetic wave vector (1,0,L=1, 3, ⋯). Figure S1D shows the measurements of magnetic order at the (1,0,1) and (0,1,1) positions. A magnetic Bragg peak was observed at the (1,0,1) position while no magnetic signal was detected at (0,1,1), indicating that the $BaFe_2As_2$ single crystal was completely detwinned. Above the antiferromagnetic transition temperature (T_N), the magnetic peak at (1,0,1) disappears as expected. The temperature dependence of the magnetic Bragg peak at (1,0,1) and (0,1,1) was also measured for $BaFe_2As_2$ and $BaFe_{1.915}Ni_{0.085}As_2$ (Figs. S2, A, B). Consistent with magnetic Bragg peak measurements in Fig. S1D, the $BaFe_2As_2$ was fully detwinned with most of the magnetic intensity located at (1,0,1). For the $BaFe_{1.915}Ni_{0.085}As_2$, the sample was partially detwinned with the intensity at (1,0,1) about three times larger than that at (0,1,1). In both cases, the applied pressure did not change T_N. We have also measured the effect of uniaxial pressure on structural transition of $BaFe_2As_2$. As shown in Figs. S2, C and D, the temperature dependence of the intensity at the (2,-2,0) nuclear Bragg reflection for the twinned and detwinned samples both shows a dramatic jump at T_s = 138 K arises from the neutron extinction release that occurs due to strain and domain formation related to the orthorhombic distortion, indicating that the uniaxial pressure does not change the tetragonal to orthorhombic lattice transition temperature [28,29]. In previous work [29], the measurable extinction release at temperatures well above T_s was suggested as arising from the significant structural fluctuations related to the orthorhombic distortion. If we assume this interpretation is correct, our data for the detwinned sample would suggest that uniaxial pressure pushes structural fluctuations to a temperature similar to resistivity anisotropy. Since extinction effect is typically only found for strong nuclear Bragg peaks, we do not expect to observe similar effect in weak magnetic Bragg scattering in Fig. S2A.

We also note that the (1,0,1) magnetic Bragg peak intensity in the twinned sample (Fig. S2A, green symbols) is not 1/2 of the detwinned sample. Since we must take the sample outside the cryostat to release the uniaxial pressure, the remounted sample will likely be at a slightly different location inside the neutron beam. Thus, for sharp magnetic or nuclear Bragg peaks, the measured intensity for strained and unstrained samples can only be compared approximately. However, this does not affect our experimental conclusion since the comparison of the scattering intensities at two wave vectors $\mathbf{Q}_{AF}$=(1,0,1) and (0,1,1) and their temperature dependence was done under the identical setup for each pressed or ambient-pressure case.

As the $BaFe_2As_2$ crystal was detwinned by uniaxial pressure, the low-energy spin waves were also fully “detwinned”. In a twinned sample, the spin waves show four-fold symmetry owing to the existence of twin domains as seen from our neutron time-of-flight measurements for $BaFe_2As_2$ (Fig. S3A) [31]. On warming to above $T_s=T_N$, spin excitations still obey the four-fold rotational symmetry (Fig. S3C). For a uniaxial strained $BaFe_2As_2$, on the other hand, the spin waves stem only from the antiferromagnetic wave vector $\mathbf{Q}_{AF}$ = (1,0,L), as shown in Fig. S3B. In the tetragonal state ($T > T_s = T_N$), the magnetic order disappears and the paramagnetic spin excitations of the unconstrained sample show four-fold symmetry (Fig. S3C).

Background subtraction

As in typical magnetic neutron scattering experiments, the backgrounds of constant-energy scans are temperature dependent. Raw inelastic neutron scattering data for typical constant-energy scans are shown in Fig. S4A. The solid curves in Fig. S4A are single Gaussian fits assuming a linear background. Apparently, most of the scans in our measurements are well described by a Gaussian with a linear background. Figure S4B shows the linear-background subtracted data from raw data in Fig. S4A.

Results of $BaFe_{1.88}Ni_{0.12}As_2$

Different from the parent compound (x = 0) and under-doped (x=0.085) sample, the uniaxial pressure has no effect on the C_4 rotational symmetry of the spin excitations for slightly electron over-doped $BaFe_{1.88}Ni_{0.12}As_2$ sample [40]. Figures S5, A and B show constant-energy scans at E = 6 meV below and above T_c, respectively, under the same uniaxial strain as that of the superconducting $BaFe_{1.915}Ni_{0.085}As_2$. We find that spin excitations have identical intensity at the (1,0,1) and (0,1,1) wave vectors, thus preserving the C_4 rotational symmetry of the underlying lattice. Figures S5, C and D show constant-momentum scans across T_c at (1,0,1) and (0,1,1), respectively. The temperature difference plot confirms the neutron spin resonance with identical intensity and energy (E = 7 meV) for (1,0,1) and (0, 1, 1) wave vectors [40]. Figure S5F plots the temperature dependence of the scattering intensity at $\boldsymbol{E}$ = 7 meV which proves that the applied uniaxial strain does not break the C_4 rotational symmetry of the spin excitations in the electron overdoped compound.

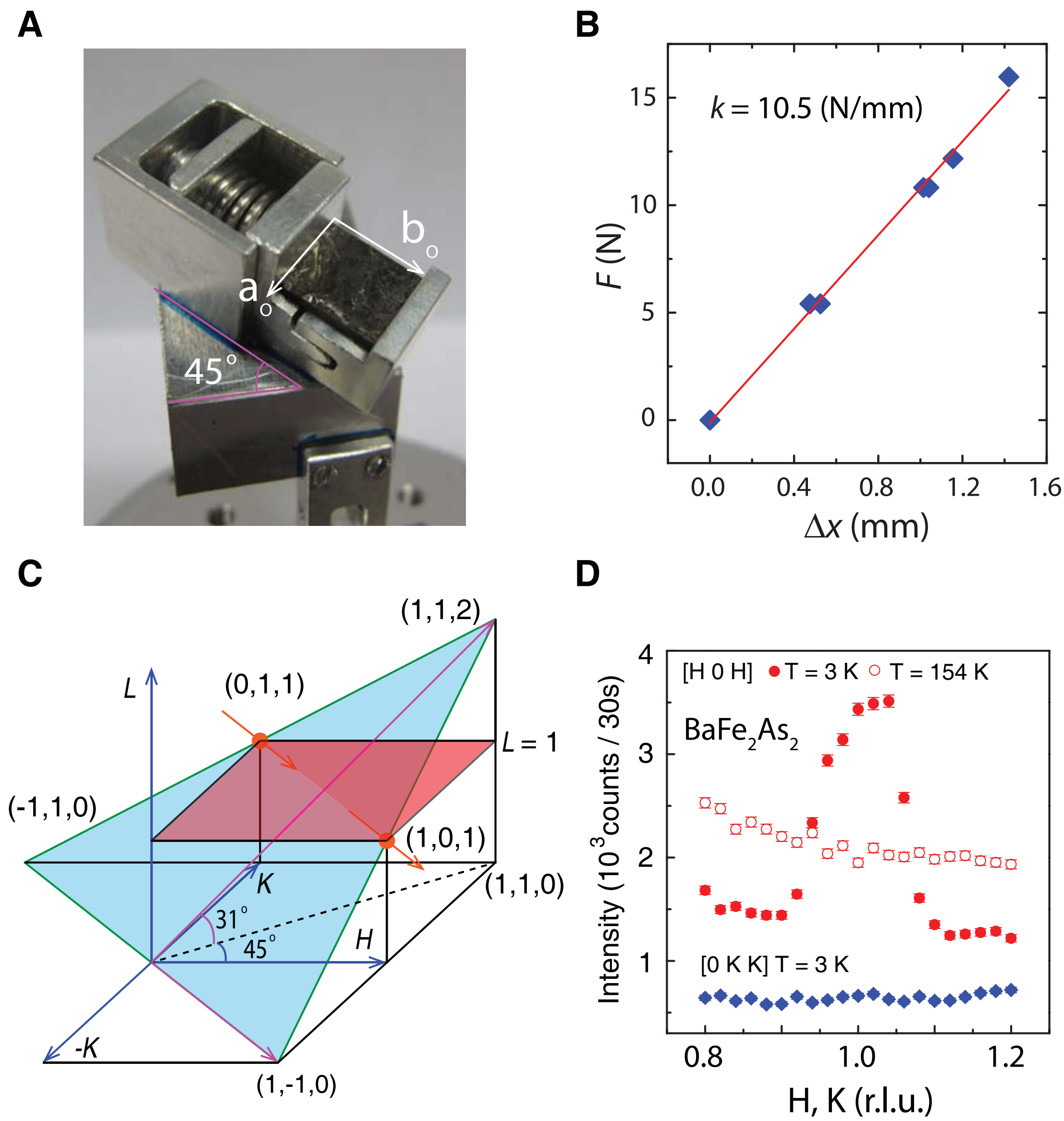

Figure S1: (**A**) Detwinning device mounted on the supporting sample holder. The crystal was aligned in the [1,0,1]×[0,1,1] scattering plane. Uniaxial pressure can be applied by a steel spring driven by a screw. (**B**) Measurement of elasticity coefficient of the spring. (**C**) The light blue shaded zone is the scattering plane where $\mathbf{Q}_{\mathbf{AF}}$ = (1,0,1) and (0,1,1) can be measured and compared directly. The (1,0,1) and (0,1,1) positions are marked by orange dots. (**D**) Magnetic Bragg peaks at the (1,0,1) and (0,1,1) positions in the detwinned $BaFe_2As_2$ below and above T_N.

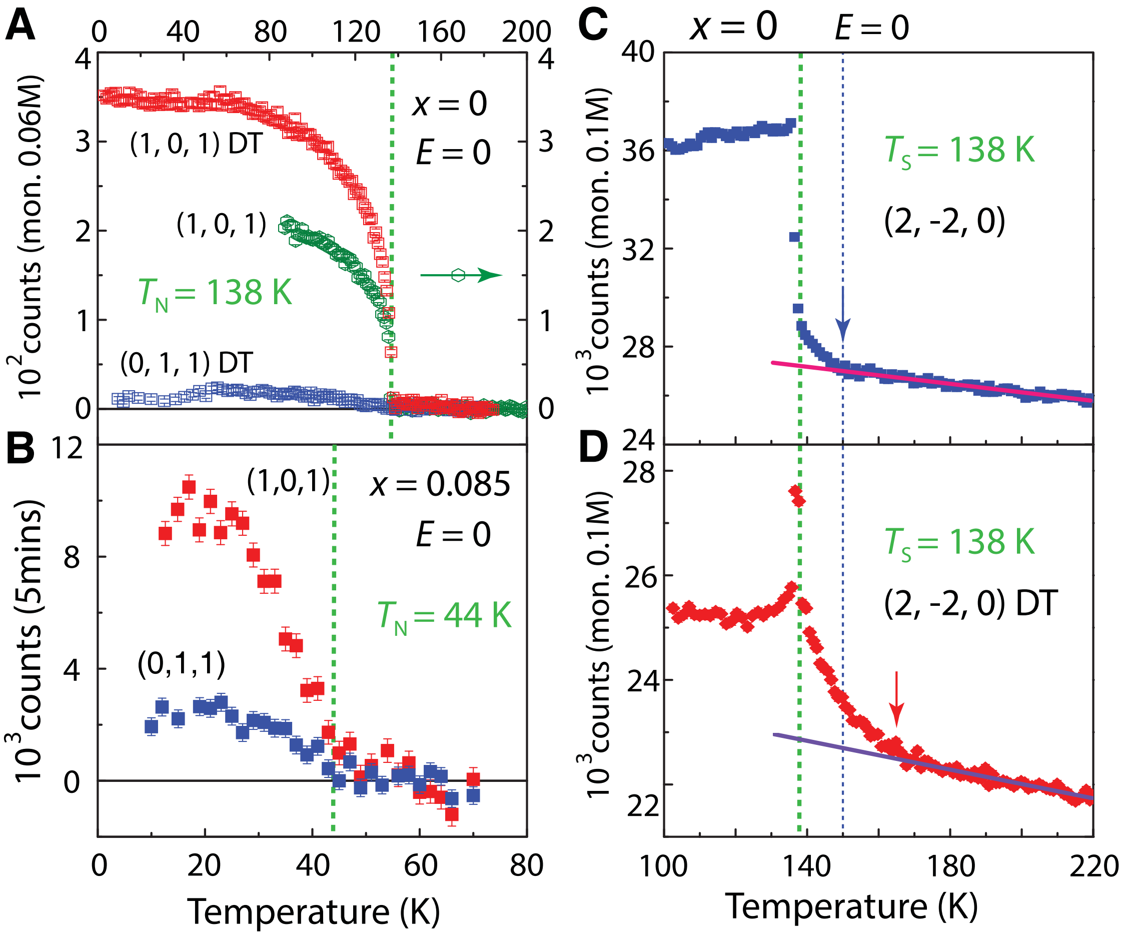

Figure S2: (**A**) Magnetic Bragg peak intensity at the (1,0,1) and (0,1,1) positions for the $BaFe_2As_2$ at zero pressure (green) and P ~ 15 MPa uniaxial pressure along the b_o axis. (**B**) Similar Bragg peaks for $BaFe_{1.915}Ni_{0.085}As_2$. (**C**) Temperature dependence of the (2,-2,0) nuclear Bragg peak at zero pressure. The sharp step at Ts is caused by releasing of the neutron extinction due to tetragonal to orthorhombic lattice distortion. (**D**) The identical scan under P ~ 15 MPa uniaxial pressure.

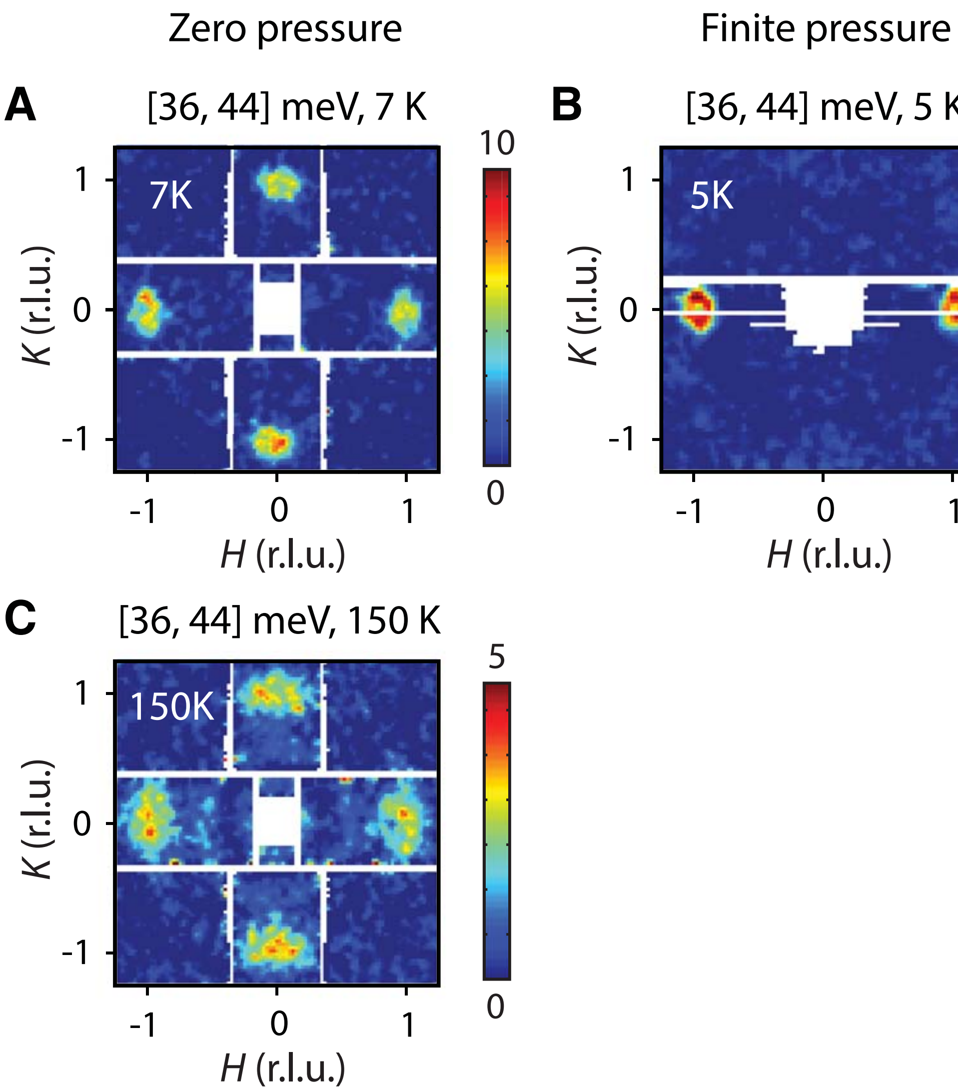

Figure S3: Comparison of the low energy spin waves for the twinned and nearly 100% detwinned $BaFe_2As_2$. (**A**) Constant energy slice of the low-energy spin waves for the twinned $BaFe_2As_2$. Data were collected on MAPS time-of-flight spectrometer with E_i = 80 meV at T = 7 K [31]. The spin waves show four-fold symmetry due to twinning. (**B**) Identical slice of the detwinned $BaFe_2As_2$ collected on MERLIN time-of-flight spectrometer with E_i = 80 meV at T = 5 K (unpublished data). Detwinning transfers the magnetic intensity from (0,1,1) to (1,0,1). (**C**) At temperature T = 150 K > T_N, the paramagnetic spin excitations of the twinned sample show four-fold symmetry, consistent with the four-fold symmetry of the underlying tetragonal lattice.

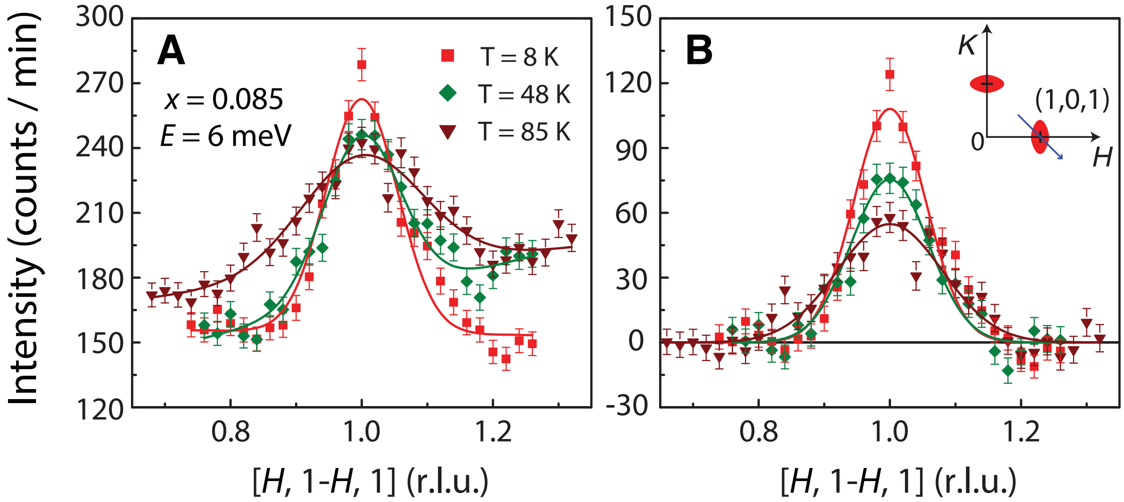

Figure S4: Background subtraction of inelastic neutron scattering data. (**A**) The raw data of the transverse scan across the (1,0,1) position. The scan trajectory is shown in the inset of (**B**). The solid curves are Gaussian fits of the data on linear backgrounds. (**B**) The linear-background subtracted data.

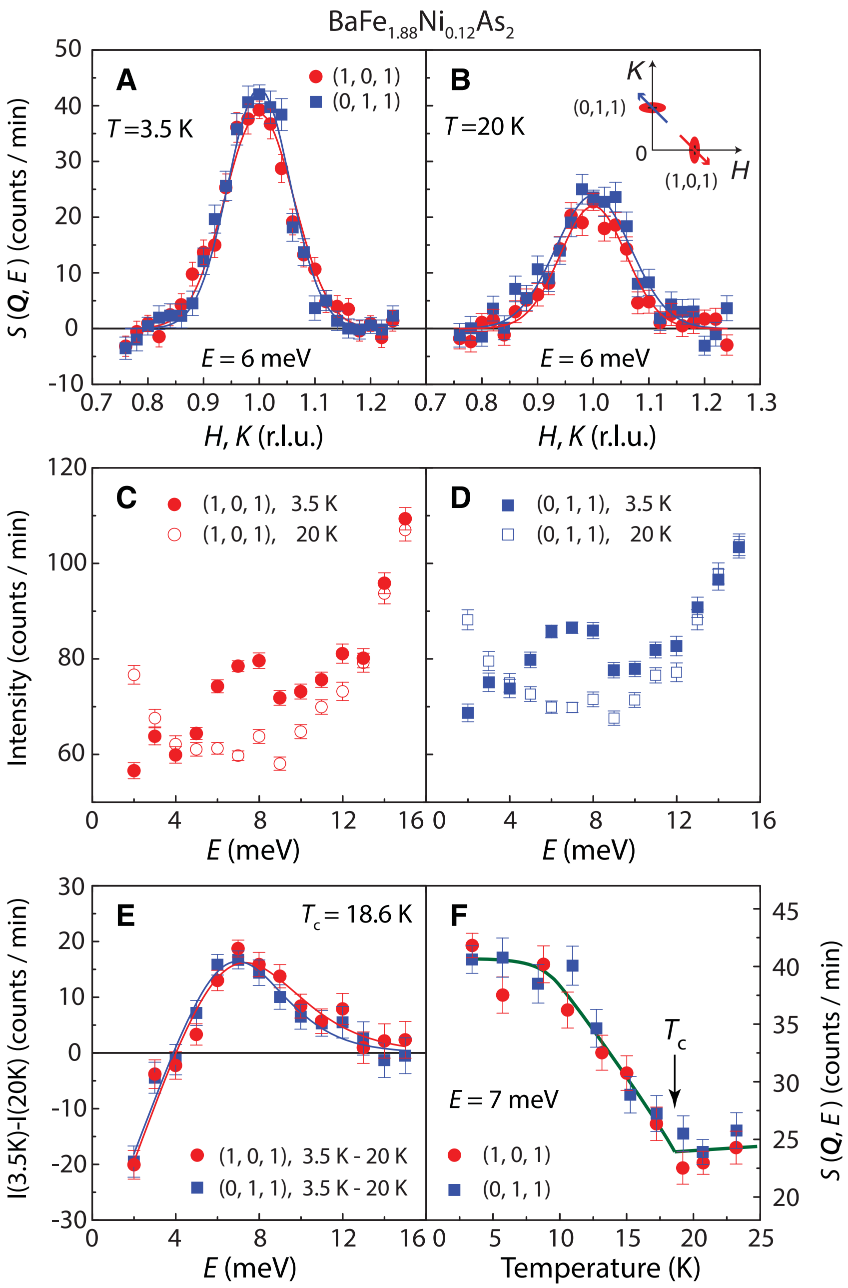

Figure S5: Temperature dependence of spin excitations at (1,0,1) and (0,1,1) for $BaFe_{1.88}Ni_{0.12}As_2$ [40]. (**A**) Linear background subtracted **Q**-scans around (1,0,1) and (0,1,1) at E = 6 meV and 3.5 K. (**B**) Identical scans at 20 K. The inset shows the trajectory of the scans. Constant **Q**-scans at (**C**) (1,0,1) and (**D**) (0,1,1) below and above T_c. (**E**) Temperature difference plot showing neutron spin resonance at (1,0,1) and (0,1,1). (**F**) Temperature dependence of the scattering at the resonance energy at (1,0,1) and (0,1,1).

References

1. Y. Kamihara, T. Watanabe, M. Hirano, H. Hosono, Iron-based layered superconductor $La[O_{1-x}F_x]FeAs$ (x = 0.05-0.12) with T_c = 26 K. *J. Am. Chem. Soc.* **130**, 3296–3297 (2008). Medline doi:10.1021/ja800073m

2. G. R. Stewart, Superconductivity in iron compounds. *Rev. Mod. Phys.* **83**, 1589–1652 (2011). doi:10.1103/RevModPhys.83.1589

3. P. C. Dai, J. Hu, E. Dagotto, Magnetism and its microscopic origin in iron-based high-temperature superconductors. *Nat. Phys.* **8**, 709–718 (2012). doi:10.1038/nphys2438

4. C. de la Cruz, Q. Huang, J. W. Lynn, J. Li, W. Ratcliff II, J. L. Zarestky, H. A. Mook, G. F. Chen, J. L. Luo, N. L. Wang, P. Dai, Magnetic order close to superconductivity in the iron-based layered $LaO_{1-x}F_xFeAs$ systems. *Nature* **453**, 899–902 (2008). Medline doi:10.1038/nature07057

5. Q. Huang, Y. Qiu, W. Bao, M. A. Green, J. W. Lynn, Y. C. Gasparovic, T. Wu, G. Wu, X. H. Chen, Neutron-diffraction measurements of magnetic order and a structural transition in the parent $BaFe_2As_2$ compound of FeAs-based high-temperature superconductors. *Phys. Rev. Lett.* **101**, 257003 (2008). Medline doi:10.1103/PhysRevLett.101.257003

6. M. G. Kim, R. M. Fernandes, A. Kreyssig, J. W. Kim, A. Thaler, S. L. Bud'ko, P. C. Canfield, R. J. McQueeney, J. Schmalian, A. I. Goldman, Character of the structural and magnetic phase transitions in the parent and electron-doped $BaFe_2As_2$ compounds. *Phys. Rev. B* **83**, 134522 (2011). doi:10.1103/PhysRevB.83.134522

7. J. H. Chu, J. G. Analytis, K. De Greve, P. L. McMahon, Z. Islam, Y. Yamamoto, I. R. Fisher, In-plane resistivity anisotropy in an underdoped iron arsenide superconductor. *Science* **329**, 824–826 (2010). Medline doi:10.1126/science.1190482

8. M. A. Tanatar, E. C. Blomberg, A. Kreyssig, M. G. Kim, N. Ni, A. Thaler, S. L. Bud'ko, P. C. Canfield, A. I. Goldman, I. I. Mazin, R. Prozorov, Uniaxial-strain mechanical detwinning of $CaFe_2As_2$ and $BaFe_2As_2$: Optical and transport study. *Phys. Rev. B* **81**, 184508 (2010). doi:10.1103/PhysRevB.81.184508

9. J. H. Chu, H.-H. Kuo, J. G. Analytis, I. R. Fisher, Divergent nematic susceptibility in an iron arsenide superconductor. *Science* **337**, 710–712 (2012). Medline doi:10.1126/science.1221713

10. I. R. Fisher, L. Degiorgi, Z. X. Shen, In-plane electronic anisotropy of underdoped '122' Fe-arsenide superconductors revealed by measurements of detwinned single crystals. *Rep. Prog. Phys.* **74**, 124506 (2011). doi:10.1088/0034-4885/74/12/124506

11. E. Fradkin, S. A. Kivelson, M. J. Lawler, J. P. Eisenstein, A. P. Mackenzie, Nematic Fermi fluids in condensed matter physics. *Annu. Rev. Condens. Matter Phys.* **1**, 153–178 (2010). doi:10.1146/annurev-conmatphys-070909-103925

12. R. M. Fernandes, A. V. Chubukov, J. Schmalian, What drives nematic order in iron-based superconductors? *Nat. Phys.* **10**, 97–104 (2014). doi:10.1038/nphys2877

13. C. Fang, H. Yao, W.-F. Tsai, J. P. Hu, S. A. Kivelson, Theory of electron nematic order in LaFeAsO. *Phys. Rev. B* **77**, 224509 (2008). doi:10.1103/PhysRevB.77.224509

14. J. Dai, Q. Si, J. X. Zhu, E. Abrahams, Iron pnictides as a new setting for quantum criticality. *Proc. Natl. Acad. Sci. U.S.A.* **106**, 4118–4121 (2009). Medline doi:10.1073/pnas.0900886106

15. M. P. Allan, T.-M. Chuang, F. Massee, Y. Xie, N. Ni, S. L. Bud'ko, G. S. Boebinger, Q. Wang, D. S. Dessau, P. C. Canfield, M. S. Golden, J. C. Davis, Anisotropic impurity states, quasiparticle scattering and nematic transport in underdoped $Ca(Fe_{1-x}Co_x)_2As_2$. *Nat. Phys.* **9**, 220–224 (2013). doi:10.1038/nphys2544

16. S. Ishida, M. Nakajima, T. Liang, K. Kihou, C. H. Lee, A. Iyo, H. Eisaki, T. Kakeshita, Y. Tomioka, T. Ito, S. Uchida, Anisotropy of the in-plane resistivity of underdoped $Ba(Fe_{1-x}Co_x)_2As_2$ superconductors induced by impurity scattering in the antiferromagnetic orthorhombic phase. *Phys. Rev. Lett.* **110**, 207001 (2013). doi:10.1103/PhysRevLett.110.207001

17. M. Yi, D. Lu, J.-H. Chu, J. G. Analytis, A. P. Sorini, A. F. Kemper, B. Moritz, S.-K. Mo, R. G. Moore, M. Hashimoto, W.-S. Lee, Z. Hussain, T. P. Devereaux, I. R. Fisher, Z.-X. Shen, Symmetry-breaking orbital anisotropy observed for detwinned $Ba(Fe_{1-x}Co_x)_2As_2$ above the spin density wave transition. *Proc. Natl. Acad. Sci. U.S.A.* **108**, 6878–6883 (2011). doi:10.1073/pnas.1015572108

18. Y. Zhang, C. He, Z. R. Ye, J. Jiang, F. Chen, M. Xu, Q. Q. Ge, B. P. Xie, J. Wei, M. Aeschlimann, X. Y. Cui, M. Shi, J. P. Hu, D. L. Feng, Symmetry breaking via orbital-dependent reconstruction of electronic structure in detwinned NaFeAs. *Phys. Rev. B* **85**, 085121 (2012). doi:10.1103/PhysRevB.85.085121

19. C. C. Lee, W. G. Yin, W. Ku, Ferro-orbital order and strong magnetic anisotropy in the parent compounds of iron-pnictide superconductors. *Phys. Rev. Lett.* **103**, 267001 (2009). Medline doi:10.1103/PhysRevLett.103.267001

20. F. Krüger, S. Kumar, J. Zaanen, J. van den Brink, Spin-orbital frustrations and anomalous metallic state in iron-pnictide superconductors. *Phys. Rev. B* **79**, 054504 (2009). doi:10.1103/PhysRevB.79.054504

21. W. C. Lv, J. S. Wu, P. Phillips, Orbital ordering induces structural phase transition and the resistivity anomaly in iron pnictides. *Phys. Rev. B* **80**, 224506 (2009). doi:10.1103/PhysRevB.80.224506

22. C.-C. Chen, J. Maciejko, A. P. Sorini, B. Moritz, R. R. P. Singh, T. P. Devereaux, Orbital order and spontaneous orthorhombicity in iron pnictides. *Phys. Rev. B* **82**, 100504 (2010). doi:10.1103/PhysRevB.82.100504

23. H. Luo, R. Zhang, M. Laver, Z. Yamani, M. Wang, X. Lu, M. Wang, Y. Chen, S. Li, S. Chang, J. W. Lynn, P. Dai, Coexistence and competition of the short-range incommensurate antiferromagnetic order with the superconducting state of $BaFe_{2-x}Ni_xAs_2$. *Phys. Rev. Lett.* **108**, 247002 (2012). Medline doi:10.1103/PhysRevLett.108.247002

24. X. Lu, H. Gretarsson, R. Zhang, X. Liu, H. Luo, W. Tian, M. Laver, Z. Yamani, Y. J. Kim, A. H. Nevidomskyy, Q. Si, P. Dai, Avoided quantum criticality and magnetoelastic coupling in $BaFe_{2-x}Ni_xAs_2$. *Phys. Rev. Lett.* **110**, 257001 (2013). Medline doi:10.1103/PhysRevLett.110.257001

25. C. Dhital, Z. Yamani, W. Tian, J. Zeretsky, A. S. Sefat, Z. Wang, R. J. Birgeneau, S. D. Wilson, Effect of uniaxial strain on the structural and magnetic phase transitions in $BaFe_2As_2$. *Phys. Rev. Lett.* **108**, 087001 (2012). Medline doi:10.1103/PhysRevLett.108.087001

26. Yu. Song, S. V. Carr, X. Lu, C. Zhang, Z. C. Sims, N. F. Luttrell, S. Chi, Y. Zhao, J. W. Lynn, P. Dai, Uniaxial pressure effect on structural and magnetic phase transition in NaFeAs and its comparison with as-grown and annealed $BaFe_2As_2$. *Phys. Rev. B* **87**, 184511 (2013). doi:10.1103/PhysRevB.87.184511

27. Materials and methods are available as supplementary materials on *Science* Online.

28. C. Lester, J.-H. Chu, J. Analytis, S. C. Capelli, A. Erickson, C. Condron, M. Toney, I. Fisher, S. Hayden, Neutron scattering study of the interplay between structure and magnetism in $Ba(Fe_{1-x}Co_x)_2As_2$. *Phys. Rev. B* **79**, 144523 (2009). doi:10.1103/PhysRevB.79.144523

29. A. Kreyssig, M. G. Kim, S. Nandi, D. K. Pratt, W. Tian, J. L. Zarestky, N. Ni, A. Thaler, S. L. Bud'ko, P. C. Canfield, R. J. McQueeney, A. I. Goldman, Suppression of antiferromagnetic order and orthorhombic distortion in superconducting $Ba(Fe_{0.961}Rh_{0.039})_2As_2$. *Phys. Rev. B* **81**, 134512 (2010). doi:10.1103/PhysRevB.81.134512

30. J. T. Park, G. Friemel, T. Loew, V. Hinkov, Y. Li, B. H. Min, D. L. Sun, A. Ivanov, A. Piovano, C. T. Lin, B. Keimer, Y. S. Kwon, D. S. Inosov, Similar zone-center gaps in the low-energy spin-wave spectra of $Na_{1-\delta}FeAs$ and $BaFe_2As_2$. *Phys. Rev. B* **86**, 024437 (2012). doi:10.1103/PhysRevB.86.024437

31. L. W. Harriger, H. Q. Luo, M. S. Liu, C. Frost, J. P. Hu, M. R. Norman, P. Dai, Nematic spin fluid in the tetragonal phase of $BaFe_2As_2$. *Phys. Rev. B* **84**, 054544 (2011). doi:10.1103/PhysRevB.84.054544

32. M. Nakajima, S. Ishida, Y. Tomioka, K. Kihou, C. H. Lee, A. Iyo, T. Ito, T. Kakeshita, H. Eisaki, S. Uchida, Effect of Co doping on the in-plane anisotropy in the optical spectrum of underdoped $Ba(Fe_{1-x}Co_x)_2As_2$. *Phys. Rev. Lett.* **109**, 217003 (2012). Medline doi:10.1103/PhysRevLett.109.217003

33. M. Y. Wang, H. Luo, M. Wang, S. Chi, J. A. Rodriguez-Rivera, D. Singh, S. Chang, J. W. Lynn, P. Dai, Magnetic field effect on static antiferromagnetic order and spin excitations in the underdoped iron arsenide superconductor $BaFe_{1.92}Ni_{0.08}As_2$. *Phys. Rev. B* **83**, 094516 (2011). doi:10.1103/PhysRevB.83.094516

34. P. Chandra, P. Coleman, A. I. Larkin, Ising transition in frustrated Heisenberg models. *Phys. Rev. Lett.* **64**, 88–91 (1990). Medline doi:10.1103/PhysRevLett.64.88

35. R. M. Fernandes, J. Schmalian, Manifestations of nematic degrees of freedom in the magnetic, elastic, and superconducting properties of the iron pnictides. *Supercond. Sci. Technol.* **25**, 084005 (2012). doi:10.1088/0953-2048/25/8/084005

36. The Ginzburg–Landau action up to the 4th power of $\mathbf{M}_{1/2}$: $S_0[\mathbf{M}_1^2, \mathbf{M}_2^2] = \iint d\mathbf{q}d\omega(r_0 + \mathbf{q}^2 + \gamma|\omega|)(\mathbf{M}_1^2 + \mathbf{M}_2^2) + u(\mathbf{M}_1^2 + \mathbf{M}_2^2)^2$ where $r_0 \propto T - T_N$ describes distance from the Néel point.

37. H.-H. Kuo, J.-H. Chu, S. C. Riggs, L. Yu, P. L. McMahon, K. De Greve, Y. Yamamoto, J. G. Analytis, I. R. Fisher, Possible origin of the nonmonotonic doping dependence of the in-plane resistivity anisotropy of $Ba(Fe_{1-x}T_x)_2As_2$ (T =Co, Ni and Cu). *Phys. Rev. B* **84**, 054540 (2011). doi:10.1103/PhysRevB.84.054540

38. S. Kasahara, H. J. Shi, K. Hashimoto, S. Tonegawa, Y. Mizukami, T. Shibauchi, K. Sugimoto, T. Fukuda, T. Terashima, A. H. Nevidomskyy, Y. Matsuda, Electronic nematicity above the structural and superconducting transition in $BaFe_2(As_{1-x}P_x)_2$. *Nature* **486**, 382–385 (2012). Medline doi:10.1038/nature11178

39. Y. Chen, X. Lu, M. Wang, H. Luo, S. Li, Systematic growth of $BaFe_{2-x}Ni_xAs_2$ large crystals. *Supercond. Sci. Technol.* **24**, 065004 (2011). doi:10.1088/0953-2048/24/6/065004

40. H. Q. Luo, Z. Yamani, Y. Chen, X. Lu, M. Wang, S. Li, T. A. Maier, S. Danilkin, D. T. Adroja, P. Dai, Electron doping evolution of the anisotropic spin excitations in $BaFe_{2-x}Ni_xAs_2$. *Phys. Rev. B* **86**, 024508 (2012). doi:10.1103/PhysRevB.86.024508